SOFT ROBOTS

Untethered unidirectionally crawling gels driven by asymmetry in contact forces

Aishwarya Pantula[1], Bibekananda Datta[2], Yupin Shi[2], Margaret Wang[1], Jiayu Liu[2], Siming Deng[2,3], Noah J. Cowan[2,3], Thao D. Nguyen[2,4,5], David H. Gracias[1,3,5,6,7,8,9]*

Reversible thermoresponsive hydrogels, which swell and shrink (deswell) in the temperature range of 30° to 60°C, provide an attractive material class for operating untethered soft robots in human physiological and ambient conditions. Crawling has been demonstrated previously with thermoresponsive hydrogels but required patterned or constrained gels or substrates to break symmetry for unidirectional motion. Here, we demonstrate a locomotion mechanism for unidirectionally crawling gels driven by spontaneous asymmetries in contact forces during swelling and deswelling of segmented active thermoresponsive poly(*N*-isopropylacrylamide) (pNIPAM) and passive polyacrylamide (pAAM) bilayers with suspended linkers. Actuation studies demonstrate the consistent unidirectional movement of these gel crawlers across multiple thermal cycles on flat, unpatterned substrates. We explain the mechanism using finite element simulations and by varying experimental parameters such as the linker stiffness and the number of bilayer segments. We elucidate design criteria and validate experiments using image analysis and finite element models. We anticipate that this mechanism could potentially be applied to other shape-changing locomotors.

INTRODUCTION

Stimuli-responsive, untethered gels that can traverse aqueous environments can have biomedical, microfluidic, and soft robotic applications (*1*–*3*). Compared with tethered robots that use fluidic or pneumatic signals to control their movement, untethered hydrogel robots can be mass-produced, are maneuverable in tight spaces, and can operate in the absence of wiring or external power sources (*4*). In particular, stimuli-responsive hydrogels, which can undergo volumetric phase transitions (swelling and deswelling) in response to environmental stimuli such as heat, light, pH, chemicals, biochemicals, and electromagnetic fields, are attractive materials for building untethered robots (*3*–*8*). Previously, researchers have structured these materials to create a range of shape-changing and functional transformer hydrogels such as grippers, fluidic actuators, and valves (*3*, *9*–*11*).

A relevant class of stimuli-responsive hydrogels is based on reversibly thermoresponsive poly(*N*-isopropylacrylamide) (pNIPAM). These hydrogels undergo lower critical solution temperature (LCST) transitions in the human physiological and ambient temperature range. Moreover, the LCST can be tuned by varying the side-chain length, crosslinking with compatible copolymers, or mixing with ionic liquids (*12*, *13*). Prior studies have used molding, three-dimensional (3D) printing, and stereolithography to create micro- and mesostructured pNIPAM structures capable of locomotion. For example, Maeda *et al.* (*14*) used the Belousov-Zhabotinsky oscillatory reaction to locomote a catalyst-modified pNIPAM strip at a constant temperature. Elsewhere, researchers have used inherently simple single-segment bilayers to create a variety of crawling robots (*15*–*19*). However, it has been challenging to break morphological symmetry (a fundamental requirement of directed locomotion) using just swelling and deswelling of a hydrogel bilayer. Consequently, attempts at creating bilayer hydrogel crawlers have necessitated ratcheted substrates or constrained channels to break symmetry and direct motion, limiting the applicability of these robots (*19*). Although it has been possible to break symmetry using cardiac cell–based robots, this scheme requires the patterned deposition of proteins and live cells on some parts of the robot and not others (*20*, *21*).

Here, we describe the use of systematic and asynchronous changes in robot morphology, driven by the transient swelling and deswelling of connected gel segments, to break the spatial (fore-aft) symmetry of contact forces and direct motion on flat surfaces. We show that symmetry is spontaneously broken simply by asymmetry in contact surface forces caused by the structural design of the robot without the need for additional patterning on the gel surface or substrate. We used gel bilayers with different thickness ratios and lateral dimensions to induce spatiotemporal asymmetries in swelling and deswelling. We also used a suspended linker with different stiffnesses and varied the number of bilayer segments and linker pattern to manipulate contact force asymmetry and tune robot displacement. We fabricated the robots by direct ink writing (DIW), a 3D printing technique that uses pressure-based extrusion for layer-by-layer assembly of multiple materials. We characterized the robots over multiple heating and cooling half-cycles and simulated their thermo-chemo-mechanical behavior using finite element analysis (FEA). We developed a conceptual framework for designing tunable, scalable, and versatile untethered stimuli-responsive locomotors that move unidirectionally (*10*, *22*–*29*).

[1]Department of Chemical and Biomolecular Engineering, Johns Hopkins University, Baltimore, MD 21218, USA. [2]Department of Mechanical Engineering, Johns Hopkins University, Baltimore, MD 21218, USA. [3]Laboratory for Computational Sensing and Robotics (LCSR), Johns Hopkins University, Baltimore, MD 21218, USA. [4]Hopkins Extreme Materials Institute (HEMI), Johns Hopkins University, Baltimore, MD 21218, USA. [5]Department of Materials Science and Engineering, Johns Hopkins University, Baltimore, MD 21218, USA. [6]Department of Chemistry, Johns Hopkins University, Baltimore, MD 21218, USA. [7]Department of Oncology, Johns Hopkins School of Medicine, Baltimore, MD 21205, USA. [8]Sidney Kimmel Comprehensive Cancer Center (SKCCC), Johns Hopkins School of Medicine, Baltimore, MD 21205, USA. [9]Center for MicroPhysiological Systems (MPS), Johns Hopkins School of Medicine, Baltimore, MD 21205, USA.
*Corresponding author. Email: dgracias@jhu.edu

RESULTS

Design and fabrication of multisegmented bilayer gel robots

Crawling via cycles of musculoskeletal traveling waves provides a common and effective means of locomotion for organisms across taxa, including snakes, salamanders, and inchworms (*30*–*35*). Usually, such traveling waves emerge due to a spatiotemporal pattern of descending neural commands [i.e., from a central pattern generator (*36*)] that drives muscles to create kinematic phase differences along a fore-aft body axis.

Here, we propose a locomotion strategy that exploits the geometry of actuators by engineering morphological asymmetries in lateral dimensions and thickness of bilayers to generate the requisite fore-aft phase differences during swelling and deswelling without needing to use any independent stimuli. We designed morphological gradients along the fore-aft axis of the soft robotic chassis, which lead, in turn, to gradients in actuator dynamics, ultimately instantiating a wave-like locomotor gait that only requires a single input.

We designed multisegmented robots with two bilayers of different morphology and bilayer ratios connected by a suspended linker (Fig. 1A). The bilayers were composed of a thermally responsive swelling gel (active material) and a nonswelling gel (passive material). We used DIW, an extrusion-based 3D printing technique, to fabricate our bilayers and robots. We used NIPAM as our active ink and acrylamide (AAM) as our passive ink. We made the inks by mixing the monomers with a shear-thinning additive Laponite nanoclay in water. After printing, we cross-linked the structures by ultraviolet (UV) exposure (*10*, *29*). From our differential scanning calorimetric measurements (fig. S15), we observed that the LCST of pNIPAM was 35.7°C.

We introduced a suspended central linker to couple the asymmetric bilayer segments. As opposed to a nonsuspended linker that maintains continual contact with the substrate, we could tune the contact area between the suspended linker and the substrate based on its stiffness (described later). We developed a sacrificial ink composed of an aqueous Laponite solution that supported a second gel layer during fabrication. Because Laponite did not cross-link during UV curing, it dissolved readily when the structure swelled in water to create the suspended linker (Fig. 1B).

After the sacrificial layer dissolution, we conducted thermal cycling of our robots in water by setting the temperature to 25°C for the cooling half-cycle and 60°C for the heating half-cycle (Fig. 1C). We heated the actuation setup well above the LCST to ensure that the temperature of the gel itself was above the LCST because there were thermal gradients in the water. We modified linker stiffness, morphology, and the number of bilayer segments to investigate their influence on the asymmetry and crawling displacement of the robots (Fig. 1, D and E).

The morphology of the bilayers can be tuned during swelling and deswelling

The relative transient swelling characteristics of the two bilayers were important to achieve the desired morphological asymmetry of the crawling robot. We measured the transient curvature of rectangular bilayers with varying dimensions over a thermal cycle (cooling and heating half-cycles). We used rectangular bilayers (10 mm by 15 mm) with two thicknesses of the pAAM layer (0.4

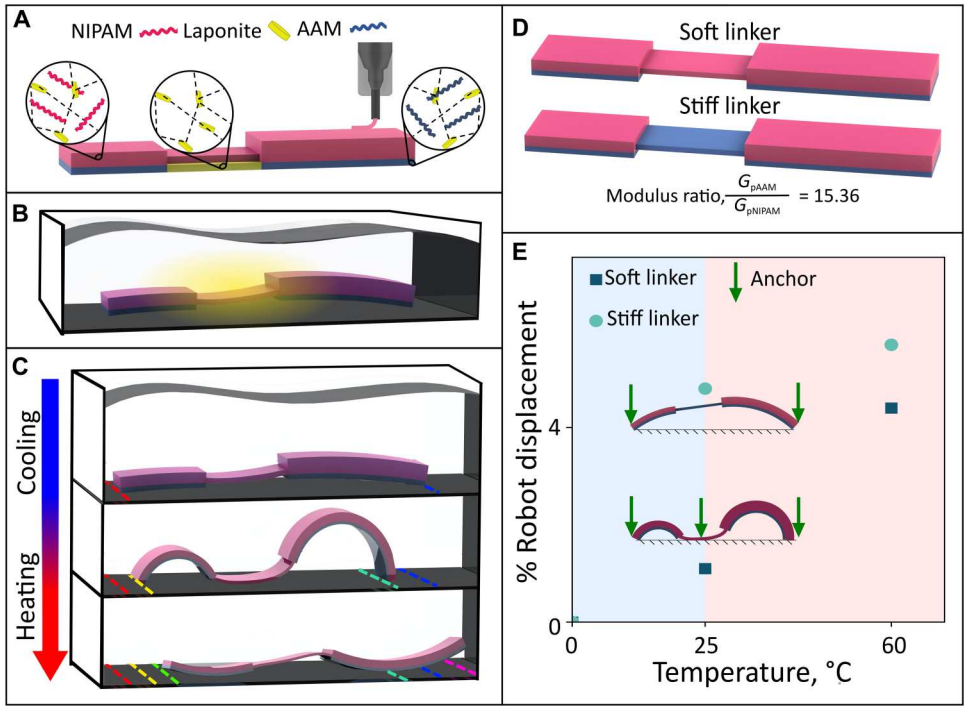

Fig. 1. Design and fabrication of multisegmented gel robots with a suspended linker. (**A**) 3D printing process. (**B**) Sacrificial layer dissolution. (**C**) Thermal actuation. One thermal cycle comprised a cooling half-cycle at 25°C and a heating half-cycle at 60°C. (**D**) Varying linker stiffnesses. (**E**) Varying the contact force distribution using linker stiffness to increase robot actuation distance during thermal cycling. The percentage of robot displacement is the distance crawled, normalized by its body length in one thermal cycle. The area shaded in blue describes the cooling half-cycle, and the area in red describes the heating half-cycle.

and 0.8 mm) and four thicknesses of the pNIPAM layer (0.4, 0.8, 1.2, and 1.6 mm). We plotted the radius of the curvature of the bilayers during the heating and cooling half-cycle against the time, t, normalized by the characteristic diffusion time, t_c, of the bilayer: $\tau = t/t_c$. We defined the characteristic diffusion time as $t_c = l_c^2/D_0$, where l_c= 1 mm is the characteristic diffusion length of the bilayer and D_0= 5 × 10^{-9} m^2/s is the self-diffusivity of water at 60°C (*37*). During the cooling half-cycle, the thinnest bilayer reached its equilibrium curvature fastest because of its smaller characteristic diffusion length. It also had the highest curvature of all the bilayers because it had the lowest bending stiffness (Fig. 2, A and B, and fig. S2). We observed that during the cooling half-cycle, the normalized swelling time varied widely (τ = 50 to 110) because of the large difference in the pNIPAM thickness across the bilayers. A thicker pNIPAM layer results in a larger characteristic diffusion length and bending modulus. During the heating half-cycle, the bilayers deswelled twice as quickly (τ = 150 to 180) (*38*).

We applied FEA of the swelling- and deswelling-induced transient bending of the bilayers to determine the swelling and deswelling properties of the hydrogels (table S2). We described the rapid deswelling of pNIPAM by modifying the constitutive model to include two different diffusivities for the swelling and deswelling process. We applied FEA to investigate the effects of material and geometric properties of the bilayer on the actuation time, defined as the time required to reach 63.2% of the equilibrium curvature (Fig. 2C). The actuation time was most sensitive to the diffusivity of the pNIPAM and the bilayer thickness ratio. Bilayers with a smaller thickness ratio and a larger diffusivity for the active material produced shorter actuation times.

The flexible linker and morphology of the bilayers break symmetry

We hypothesized that two dissimilar gel bilayer segments connected by a suspended linker would generate asymmetry in contact forces, leading to unidirectional robot displacement during thermal cycling. We used the bilayer thermal cycling data to choose two bilayers with the greatest curvature difference. We picked a small (0.8-mm pNIPAM–0.4-mm pAAM) bilayer and a large (1.2-mm pNIPAM–0.4-mm pAAM) bilayer and connected them with a suspended flexible pNIPAM linker. The specific lateral and thickness dimensions of the robot are in fig. S4A. We thermally stimulated the robot in water by switching the temperature between 25° and 60°C.

During the cooling half-cycle, the robot was allowed to swell from its cured state at 60°C to room temperature (25°C), and we observed swelling-induced bending in both bilayer segments. Simultaneously, the suspended linker swelled and sagged to touch the underlying surface along with the outer edge of both bilayers. This sagging caused the linker to act as an anchor and move the bilayers toward it by the end of the half-cycle (Fig. 3A, i to iii). Once we switched to the heating half-cycle, the robot transitioned from its swollen-bent state to a deswollen-flattened state (collapsed state) (Fig. 3A, iii to v). The linker straightened and achieved its original suspended state, whereas the two bilayers deswelled asynchronously. During deswelling, because of the size and curvature asymmetry between the larger and smaller bilayer, the anchor was transferred from the linker to the larger bilayer. As a result, the robot moved unidirectionally as the small bilayer and linker were drawn toward the larger bilayer.

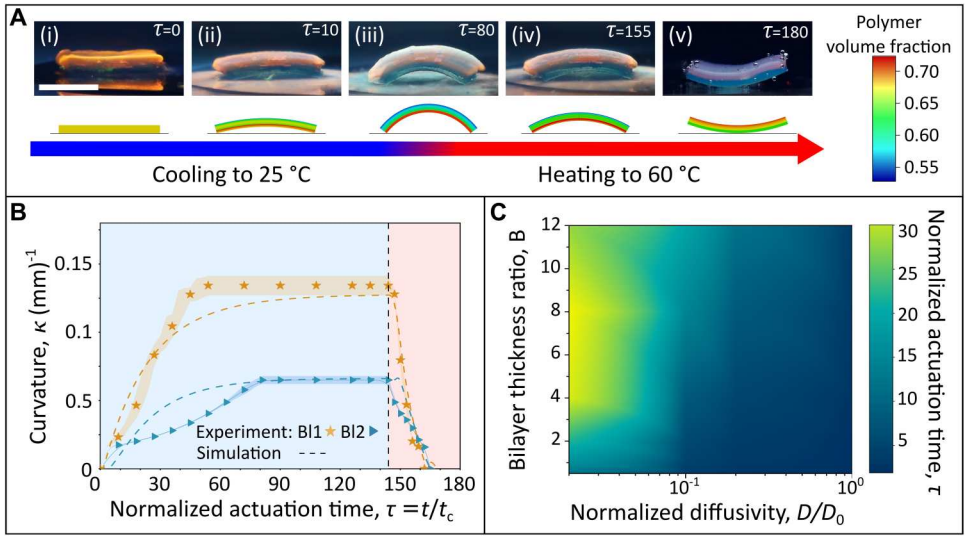

Fig. 2. Tuning actuation time and curvature of the bilayers by varying thickness ratio during thermal cycling. (**A**) Experimental images and simulation snapshots of the bending of the 0.8-mm pNIPAM–0.4-mm pAAM bilayer versus normalized actuation time defined as $\tau = t/t_c$, (where $t_c = l_c^2/D_o$, l_c = 1 mm, $D_0 = 5 \times 10^{-9}$ m^2/s). The images were taken during one thermal cycle by first cooling to 25°C (i to iii) and then heating to 60°C (iv and v) more than 10 hours. D_0 is the self-diffusivity of water at 60°C (*37*). The bilayer deswelled beyond its cured state and achieved negative curvature at the end of heating (v) τ = 180. Scale bar, 10 mm (i). The color scaling gradient indicates the polymer volume fraction from the finite element simulations, with lower numbers indicating larger swelling. The polymer volume fractions at the cured state, fully swollen at 25°C, and fully deswollen state at 60°C were 0.67, 0.59, and 0.72, respectively. (**B**) Plot of the curvature of the 0.8-mm pNIPAM–0.4-mm pAAM bilayer (Bl1) and 0.8-mm pNIPAM–0.8-mm pAAM bilayer (Bl2) observed over normalized actuation time during the cooling (blue area) and heating (red area) half-cycles. Both bilayers fully swelled by τ = 80 and deswelled by τ = 165. The data points are from experiments with the shading representing the SD with a sample size of three. The dashed lines represent the fitted model from simulations. (**C**) Plot of the normalized actuation time versus bilayer thickness ratio, $B = h_{pNIPAM}/h_{pAAM}$, and normalized diffusivity, D/D_0.

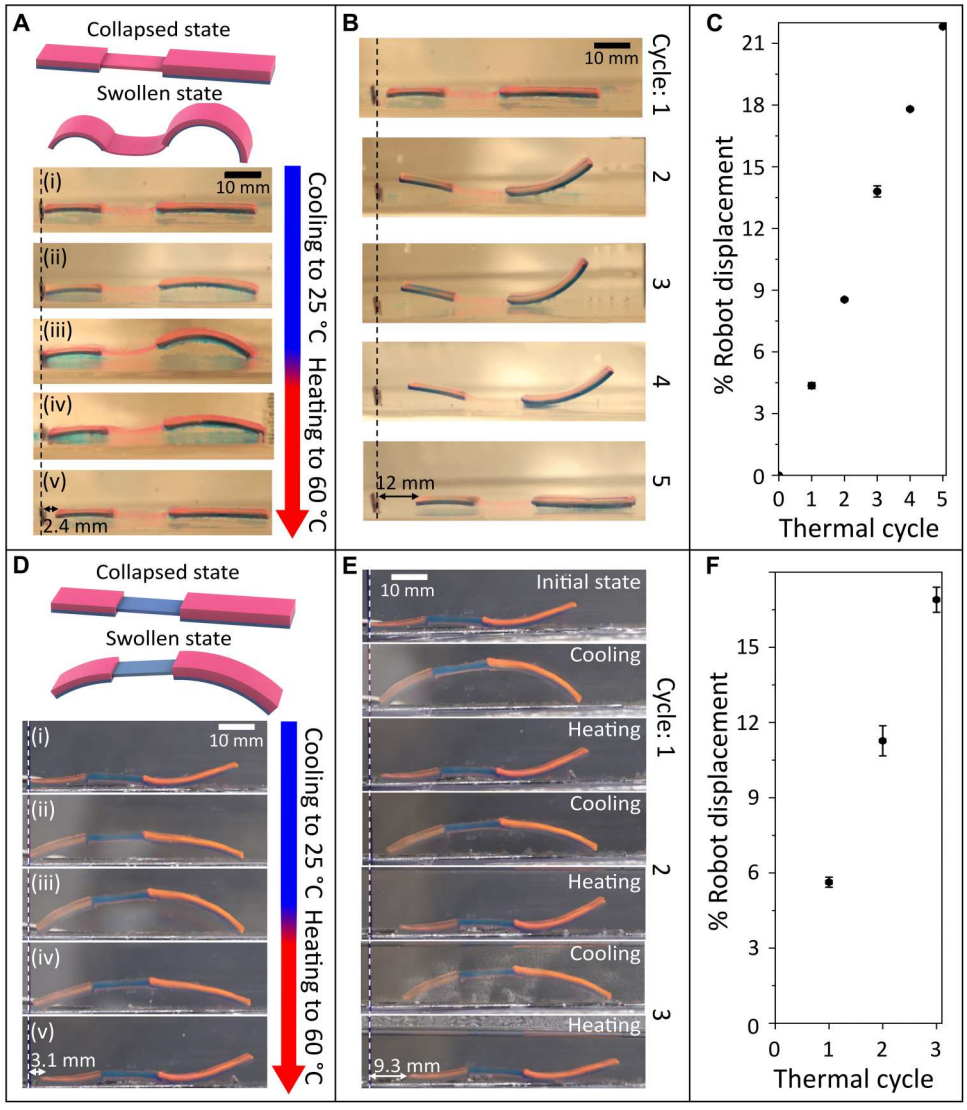

Fig. 3. Thermal cycling of two-segment robots with a flexible or a stiff linker. (A to C) Robot with a flexible pNIPAM linker. (**A**) Experimental images of the robot across one thermal cycle consisting of one cooling/heating half-cycle. (i to iii) Cooling half-cycle: (i) cured state, (ii) intermediate state, and (iii) swollen state. (iv and v). Heating half-cycle: (iv) intermediate state and (v) deswollen state of robot. (**B**) Experimental images of the robot observed at the end of each of five thermal cycles. (**C**) Plot of the percentage of robot displacement at the end of each thermal cycle. This robot with a flexible linker crawled 12 mm after five cycles, which is equivalent to 4.4% body length per cycle. (D to F) Robot with a stiff pAAM linker. (**D**) Experimental images of the robot across one thermal cycle consisting of one cooling/heating half-cycle. Cooling half-cycle: (i) cured state, (ii) intermediate state, and (iii) swollen state. Heating half-cycle: (iv) intermediate state and (v) deswollen state of robot. (**E**) Experimental images of the robot observed at the end of each of three thermal cycles. (**F**) Plot of the percentage of robot displacement at the end of each thermal cycle. This robot with the stiff linker crawled 9.3 mm in three cycles, which is equivalent to 5.6% body length per cycle. Error bars in (C) and (F) indicate the SD with a sample size of three.

We subjected this robot to five thermal cycles and measured the displacement of the robot after each cycle (Fig. 3, B and C). We observed that our robot crawled consistently in the direction of the larger bilayer, moving about 4.4% body length per cycle. The final curvature of the robot segments varied slightly with each cycle, likely due to differences in the reorganization of the molecular chains of the cross-linked polymer and hydrogen bonding that occur between heating and cooling half-cycles. In addition, the pNIPAM layer deswelled beyond its cured state length and caused the bilayers to bend in the opposite direction as compared with its swollen state (*39*).

Varying the linker stiffness speeds up the gel crawler

We hypothesized that the stiffness of the linker would strongly influence the morphology and, consequently, the gait and contact forces of the robot. To study this effect, we printed the same two-segment robot with identical dimensions but replaced the flexible pNIPAM linker with a stiff pAAM linker (Fig. 3, D to F). During the cooling half-cycle, the stiff linker held its flat shape. The stiff linker remained suspended between the bilayers and did not play any role in anchoring. As a result, there was an increase in the net contact force asymmetry between the larger and smaller bilayers, and the unidirectional displacement increased from 4.4 to 5.6% body length per cycle (movie S1), proving our hypothesis.

We also confirmed that the locomotion direction of the robots depends on the relative orientation of the small and large bilayers. We thermally stimulated both the flexible and stiff linker robots over 20 thermal cycles and observed consistent unidirectional motion in the direction of the larger bilayer (fig. S4, B and D).

Asymmetry in contact forces generates unidirectional motion

We obtained insight into our experimental findings by performing FEA of the thermochemomechanical behavior of the robot during thermal cycling. The constitutive model by Chester *et al.* (*40*) assumed that the hydrogel was in a dry polymer state at the beginning of the simulation. In contrast, the hydrogels that we fabricated by DIW were in a partially swollen state. To achieve this initial swollen configuration, we simulated the free swelling of both the pNIPAM and pAAM materials at a reference temperature of 50°C as described in the Supplementary Materials. The effects of gravity and buoyancy were prescribed by applying a body force, $b_y = \Delta\rho g$, where $\Delta\rho = 100$ kg/m^3 is the difference in the density between the polymer and water and g is the gravitational acceleration. We discretized the bottom surfaces of all three segments of the robot (fig. S11) using contact surface elements. We assumed a rigid surface underneath the hydrogel segments to prevent interpenetration. The surface was assumed to have a frictional coefficient, $f_k = 0.1$, to describe the frictional sliding of the robot during the thermal cycle. For low sliding velocities, most literature reported the coefficient of friction of pAAM hydrogel to be below 0.1 (*41*). We chose $f_k = 0.1$ to ensure a sufficient difference in the friction force between the segments to produce locomotion.

We lowered the temperature from 50° to 25°C at a rate of 1.67°C/min and held it at 25°C for 2.45 hours and then increased the temperature to 60°C at 0.58°C/min and held it at 60°C for 2 hours to simulate the actuation experiments. This temperature ramping caused the thermally responsive pNIPAM to swell during the cooling half-cycle and deswell during heating half-cycle. The swelling strain mismatch between the active pNIPAM and passive pAAM hydrogel caused the bilayer segments to curve downward during cooling, pushing the pNIPAM linker into contact with the surface.

The left edge of the smaller bilayer moved to the right, and the right edge of the larger bilayer moved to the left (Fig. 4A). The opposing motion of the bilayer segment resulted in a minimal 0.1% translation of the center of the linker of the robot. The mismatch in the deswelling strain between pNIPAM and pAAM caused the robot to curve upward during heating. The curving/bending of the larger bilayer and deswelling of the linker pulled the robot to the right and caused a net displacement of 1.1% body length over the thermal cycle (Fig. 4B).

We plotted the normal force (the force perpendicular to the contact surface) acting on the two bilayer segments and linker to understand the mechanism of forward translation of the hydrogel robot (Fig. 4C). We calculated this by summing the nodal normal forces on the contact surface of an individual segment. The normal force scales with the magnitude of the friction force as the inverse of the Coulomb friction coefficient.

Initially, the normal force was highest for the larger bilayer because it was the largest segment in the robot. During cooling, the bending of the bilayers pushed the linker down on the surface, which caused it to experience the largest normal force and, thus, the largest friction force. The normal force acting on the bilayers decreased by about 50%. At the same time, the normal force increased by more than four times than for the linker. The higher normal force caused the linker to act as an anchor and the center of both bilayers to move toward the linker. Increasing the temperature to 60 °C caused both bilayers first to straighten and then curl upward, lifting the linker from the contact surface. The larger bilayer was displaced by −0.1 mm during heating, whereas the smaller bilayer was displaced by 0.63 mm (Fig. 4A). Once again, the larger bilayer experienced the largest friction force of the three segments and acted as an anchor, allowing the smaller bilayer and linker to slide to the right, producing a net forward motion (movie S2).

We performed three additional finite element simulations to validate the hypothesis for the mechanism of the robot locomotion. First, we repeated the finite element simulation on a frictionless contact surface ($f_k = 0.0$). The robot experienced no net translation (fig. S13). We next changed the frictional anchoring of the robot by switching the positions of the smaller and larger bilayers to produce net motion in the opposite direction. Having the larger bilayer on the left relocated the anchoring point during heating to the left and caused the smaller bilayer to slide to the left, producing a net motion to the left. The stroke (net motion) of the robot was the same in magnitude but opposite in direction as the baseline case, and the friction forces acting on the larger and smaller bilayers and the linker were the same as for the baseline case. We observed the same behavior in our experiments when we turned our flexible linker robot around, thermally stimulated it, and observed it crawl in the opposite direction (movie S3). We elaborate more on these studies in the Supplementary Materials (fig. S14).

Last, we changed the design of the robot by replacing the pNIPAM linker with a stiffer passive hydrogel linker. We simulated the motion of a robot with a linker that was four times shorter and about 46 times stiffer during the cooling half-cycle (Fig. 4D). The bending of the bilayers during cooling lifted the linker from the contact surface, creating an asymmetric arch. We observed that the point of contact of the larger bilayer, point Y, was displaced by 2.1%. In contrast, the point of contact of the smaller bilayer, point X, was displaced by a substantially larger amount, 20.3%, in the opposite direction (Fig. 4E). The normal force was larger at point Y for the larger bilayer than at the contact point X for the smaller bilayer. This asymmetry in contact forces caused point Y to act as an anchor, and the robot translated to the right during the cooling half-cycle (Fig. 4F). The trend observed in our simulations that a robot with a stiffer linker shows higher unidirectional displacement agrees with the experimental observations (Fig. 3).

Alternating linker patterns and adding bilayer segments increases displacement

We studied the dependence of the number of bilayer segments and the linker pattern on the morphology and displacement of gel crawlers. We hypothesized that these factors would induce a larger asymmetry between the bilayer segments, increasing the displacement of the robot. We varied the number of bilayer segments of the robots from two to four (Fig. 5, A and D, and figs. S5 and S6). Taking inspiration from an accordion, we also redesigned the linker from the fully pNIPAM or pAAM composition (Fig. 3) to a combination of alternating pAAM and pNIPAM strips, as shown in Fig. 5. We hypothesized that the alternating geometry would allow the linker to

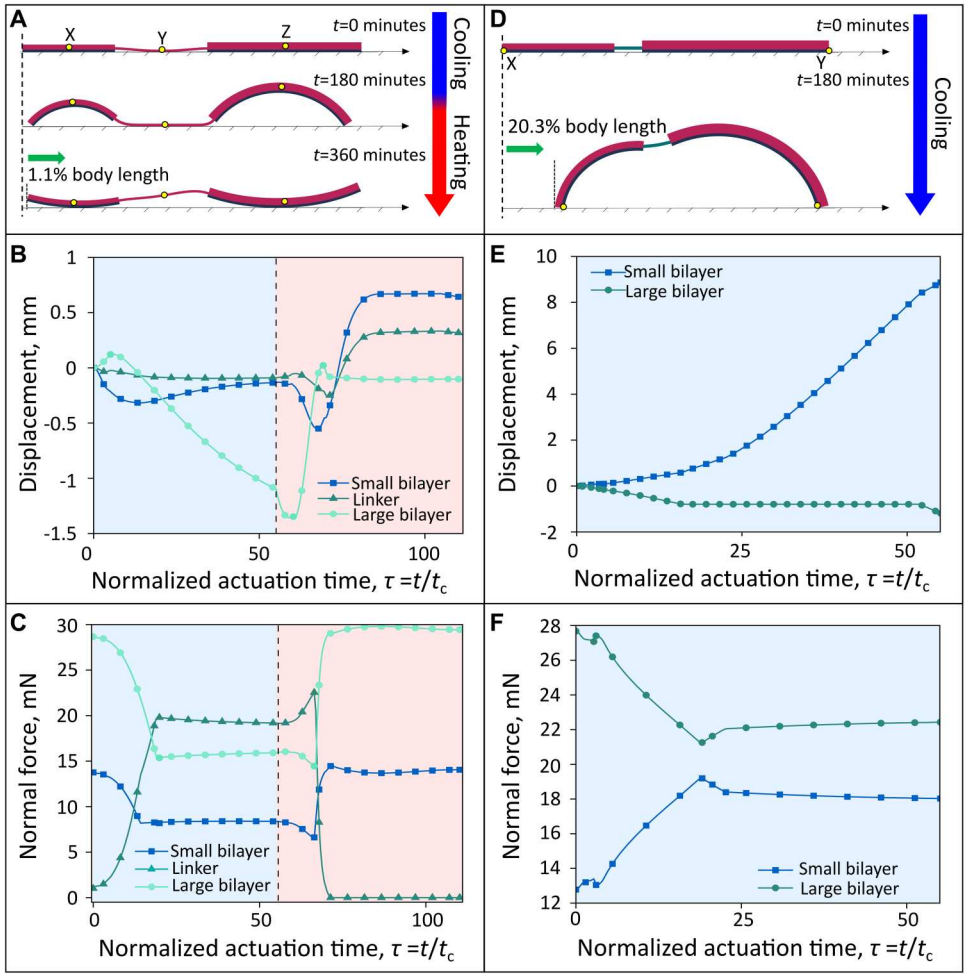

Fig. 4. FEA of a two-segment robot with different linkers. (A to C) Robot with a flexible linker. (**A**) The deformed shape of the crawling robot upon cooling (t= 180 min) and heating (t = 360 minutes). (**B**) A plot of the lateral displacement of the center of the bilayers and the linker versus normalized time for cooling (blue area) and heating (red area) half-cycles. (**C**) A plot of the normal force (the force perpendicular to the contact surface) exerted by different segments on the contact surface versus normalized actuation time. (D to F) Robot with a short and stiff linker. (**D**) The deformed shape of the robot with the smaller bilayer moving toward the larger bilayer upon cooling. (**E**) A plot of lateral displacement of the outer edges of the bilayers versus normalized actuation time. (**F**) A plot of the normal force on the contact surface exerted by the bilayers versus normalized actuation time.

elongate while maintaining its shape. We stimulated all the robots across multiple thermal cycles, and the results are discussed below.

First, we 3D-printed a three-segment robot with an alternating linker (fig. S5A). This gel robot consisted of two small and one large bilayer segment connected by a linker composed of five stripes of pAAM and six stripes of pNIPAM. During the cooling half-cycle, the linker elongated and had minimal anchoring to the contact surface, effectively behaving like a stiff linker (Fig. 5A). During the heating half-cycle, an asymmetry was induced both by the morphological differences in the bilayer curvature and the uneven distribution of the two small bilayer segments. We observed a stick-slip motion and a large displacement of 7.63% body length per cycle (movie S4). In addition, the robot moved unidirectionally toward the two smaller bilayers because of the increase in contact area on the side of the smaller bilayers. We also performed a 20–thermal cycle study on this gel robot to confirm consistent unidirectional motion (fig. S5B). We also compared its displacement to a similar robot composed of two small and one large bilayer segments but with a flexible pNIPAM linker (fig. S6). Because this linker sags and has a high contact area with the underlying surface during the cooling half-cycle, the displacement is reduced to 3.9% body length per cycle (movie S5).

Next, we 3D-printed a four-segment robot with an alternating linker (fig. S5C). This gel robot consisted of two small and two large bilayer segments connected by a linker composed of two stripes of pAAM and three stripes of pNIPAM. During the cooling half-cycle, the linker again elongated and had minimal anchoring to the contact surface, also effectively behaving like a stiff linker. Because the contact area was greater on the side of the two larger bilayers, the robot consistently moved in that direction and the displacement was high, measured at 12.2% body length per cycle (Fig. 5, C and D; fig. S5D; and movie S6). These studies confirm that we can manipulate normal force asymmetry in the robot by varying the morphology and relative contact area of the bilayers and linker.

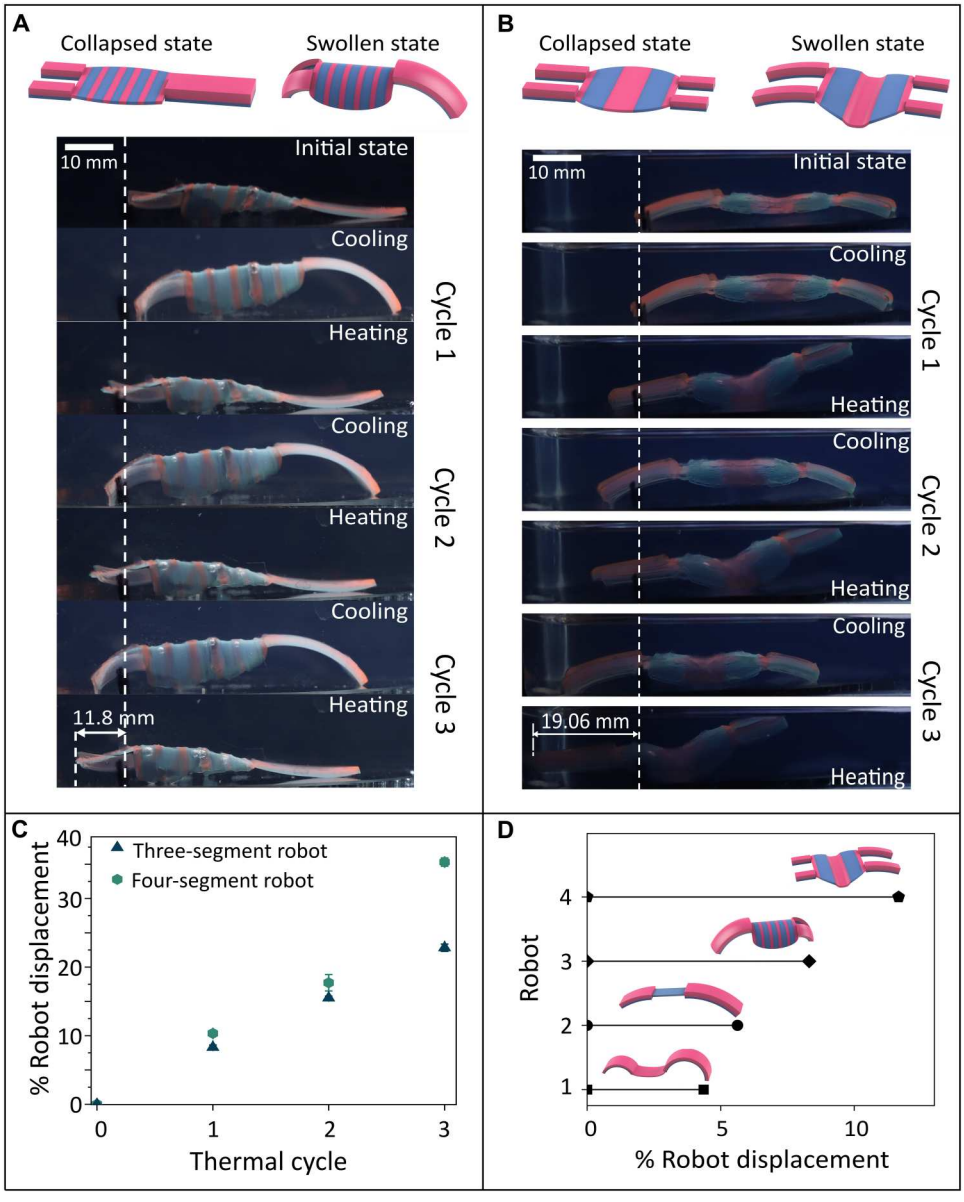

Fig. 5. Displacement of gel robots with varying bilayer segments and linker morphology. (**A**) Illustration and experimental images of a three-segment robot at the end of each heating and cooling half-cycle over three consecutive cycles. (**B**) Illustration and experimental images of a four-segment robot at the end of each heating and cooling half-cycle over three consecutive cycles. (**C**) Plot of the percentage robot displacement of the three-segment and four-segment robots over three thermal cycles. The error bars indicate the SD with a sample size of three. The three-segment robot moved 7.63% body length per cycle, whereas the four-segment robot moved 12.2% body length per cycle. (**D**) Comparison of the average percentage displacement of all the experimentally demonstrated robots.

DISCUSSION

We have described and validated a mechanism for the untethered unidirectional crawling of multisegmented gel robots on flat unpatterned substrates. The mechanism relies on a spatial morphological gradient along the fore-aft axis, which in turn generates an asymmetry in contact forces of gel segments and linkers, leading to unidirectional locomotion. Using thermal cycling of a model gel robot consisting of two bilayer segments with either a stiff or flexible linker, we characterized the mechanism experimentally and compared the results to FEA simulations with good agreement. We observed consistently that the magnitude and asymmetry of contact forces between different parts of the robot and the underlying surface are important factors that determine the extent of unidirectional displacement. In addition, these factors can be tuned by varying the dimensions and numbers of the small and large bilayers. We observed an increase in the displacement upon increasing the number of bilayers, and robots moved consistently in the direction of the bilayers with the larger contact forces.

We have also observed that the robot displacement can be controlled by varying the linker stiffness. Stiff or elongating linkers have lower contact with the underlying surface and consequently anchor less, resulting in greater contact force asymmetry between the

bilayer segments and leading to larger displacement. Thus, soft-robot design can be used to manipulate shape change and contact forces to control both direction and speed.

In terms of speed of locomotion, the time scales of swelling of gel robots are limited by diffusion and are generally slow as compared with, for example, piezoelectric or electromagnetic actuators. However, they have advantages, including being powered and operated in aqueous environments without the need for tethers or wires, which is important for locomotion in small and tortuous spaces. We also note that many soft-bodied organisms, such as worms, move slowly. Moreover, many dynamic processes in nature—such as growth, morphogenesis, disease progression, digestion, and decay—are slow processes. If needed, such gel robots could also potentially be sped up by reducing diffusion times (such as by using thinner films) or by incorporating nonlinear chemical or mechanical processes.

Although we heated and cooled the entire setup in our study, the robots have the potential to function autonomously in environments where the temperature oscillates or varies. In addition, in the future, it is conceivable that localized heating or cooling modalities could be integrated within the robot body to facilitate programmable or autonomous operation in small aqueous spaces independent of the temperature of the environment. Of note, there are several battery-operated resistive heaters and Peltier elements as well as magnetic, acoustic, or optically excitable particles that could potentially be incorporated within the gels. In terms of the operating temperature range, we note that the LCST in pNIPAM and other gels, such as blends of biocompatible poly(oligo(ethylene glycol) methyl ether methacrylate/di(ethylene glycol) methyl ether methacrylate, are widely tunable across the biological range of temperatures (*13*).

In addition to thermally responsive hydrogels, the manipulation of morphology and contact force asymmetry to tune distributed spatiotemporal dynamics of soft robots, as demonstrated in this work, could potentially be used with other stimuli-responsive materials. For example, hydrogels can swell or deswell in response to multiple stimuli, including light, pH, or DNA hairpins, and locomotion in response to these stimuli can enhance autonomy, programmability, and applicability (*3*, *42*).

MATERIALS AND METHODS

Composition of the hydrogel inks

We formulated shear-thinning hydrogel inks compatible with the DIW printing process mentioned in Fig. 1A by modifying the rheological properties of aqueous mixtures of monomers, a cross-linker, and a photoinitiator (*10*). We used NIPAM for the active ink and AAM monomer for the passive ink. The thermoresponsive pNIPAM undergoes a coil-to-globule transition above its LCST, which was measured to be 35.7°C (fig. S15), whereas pAAM shows no thermoresponsivity. We used Laponite nano clay as the rheology modifier, Irgacure 2959 as the photoinitiator, and *N*,*N*′-methylenebisacrylamide (BIS) as a cross-linker (used only for the passive AAM ink). We also added two dyes to the mixtures to increase contrast during imaging: a fluorescent rhodamine dye (emission, 568 nm) in the active ink and methylene blue in the passive ink.

Preparation of the hydrogel inks

NIPAM active ink

We blended Laponite XLG (BYK USA Inc.) with pure deionized (DI) water and an aqueous dye solution of methacryloxyethyl thiocarbamoyl rhodamine B (0.12 mg/ml; Polysciences Inc.). We homogenized the mixture using a planetary mixer (Mazerustar KK-250S, Kurabo Industry Ltd.) for about 90 s at 2100 rpm. We then added the NIPAM monomer (Scientific Polymer Irgacure-Products Inc.) and the UV photoinitiator 2-hydroxy-4′-(2-hydroxyethoxy)-2-methylpropiophenone or Irgacure 2959 [Badische Anilin und Sodafabrik (BASF)]. We homogenized the solution again for about 150 s at 2500 rpm. The relative final concentrations of the components of the active ink were 76% (w/w) pure DI water, 8.5% (w/w) NIPAM, 8.5% (w/w) aqueous rhodamine dye solution, 6.8% (w/w) Laponite, and 0.2% (w/w) Irgacure.

AAM passive ink

Similar to the active ink, we again blended Laponite with pure DI water and an aqueous dye solution of methylene blue (0.5 mg/ml; Sigma-Aldrich). We homogenized the mixture for about 90 s at 2100 rpm. We then added an AAM monomer (Sigma-Aldrich), Irgacure 2959, and the cross-linker BIS (Sigma-Aldrich). We homogenized the solution again for about 150 s at 2500 rpm. The relative final concentrations of the components of the passive ink were 74.7% (w/w) DI water, 8.3% (w/w) aqueous methlylene blue dye solution, 7.9% (w/w) AAM, 6.6% (w/w) Laponite, 1.7% (w/w) BIS, and 0.8% Irgacure.

Sacrificial ink

We blended Laponite with pure DI water to make the sacrificial ink to print the supporting layer for the suspended linker of the robot. We homogenized the mixture for about 90 s at 2100 rpm. The relative final concentrations of the sacrificial ink were 92.6% (w/w) pure DI water and 7.4% (w/w) Laponite.

After the ink homogenization, we kept the inks at room temperature to age for at least a day before use to achieve the desired rheological properties. The ink schematics and additional details are in the Supplementary Materials.

3D printing and robot curing

We first 3D-printed the bilayers or robots with the inks and later cured them after printing using UV light. For 3D printing, we generated computer-aided design and STL files using SOLIDWORKS (Dassault Systèmes) and used the Slic3r software to generate our G-code files. We used a pneumatic extrusion–based printer (Inkredible+ 3D Bioprinter, Cellink) to print our bilayers and robots. After calibrating the *XYZ* axes, we manually estimated the nozzle offset of the two printer heads by printing a calibration structure of two superimposed cylinders and incorporating it into the G-code. Because the robots were printed with three materials (NIPAM, AAM, and sacrificial ink) using a two-nozzle printer, it was necessary to modify the G-code to control the sequence in which the different segments were printed. This sequential printing allowed us to exchange the three inks in the two nozzles during the printing process.

After 3D printing the entire bilayers or robots, we cured them using two UV light-emitting diode probes (365-nm wavelength, 12-mm lens diameter) and the OmniCure UV (LX 500, Lumen Dynamics) system at 100% exposure intensity for 200 s. Because the robots were wider than the lens diameter, we cured them in sections to achieve a relatively uniform curing. More details on the printer

specifications and fabrication setup are included in the Supplementary Materials.

Study design for experimental characterization of the bilayers and robots

We designed our study to systematically investigate the effects of tunable engineering parameters such as bilayer thickness ratio, number of bilayers, and linker pattern on bilayer curvature and robot displacement. We carried out thermal cycling experiments using bilayers and robots and conducted all experiments on silicon wafers in water in the same actuation setup. The goal of each time-lapse experiment was to understand and quantify the behavior of the bilayers and the robot over thermal cycling to tune parameters for the model and establish a comparison between experiments and simulations. We have included more details of the thermal actuation of bilayers and robots below and in the Supplementary Materials.

We did robot characterization experiments over multiple (3, 5, and 20) thermal cycles, beginning with the cooling half-cycle and ending with the heating half-cycle. We performed all experiments in triplicate, and we used the data to generate error margins, as shown and mentioned in each figure legend. We used a combination of MATLAB and ImageJ to estimate parameters like the radius of curvature and robot displacement. We generated time-lapse videos of the robot actuation using Windows Movie Maker (Microsoft). We have included additional details regarding imaging and time-lapse experiments in the Supplementary Materials.

Thermal actuation of bilayers

After printing the bilayers and curing them, we placed three samples of each bilayer design in a clear plastic box (20 cm by 10 cm). We added 750 ml of DI water at room temperature to the box and used a broad-spectrum UV light source to excite the rhodamine dye in pNIPAM and to image the bilayers with a digital single lens reflex camera (Canon). After the bilayers equilibrated at 25°C, we thermally cycled the bilayers in water on a hot plate (Thermo Fisher Scientific) by switching the temperature to 60°C at 1.75°C/min for the heating half-cycle and back to 25°C at 0.8°C/min for the cooling half-cycle. We took images of the swelling and deswelling of the bilayers over 8 hours in 5-min intervals.

Thermal actuation of robots

We used the same experimental setup and conditions used for the bilayers to characterize the thermal actuation of the gel robots. We generated all the figures in the main text using three or five thermal cycles. For the statistical study of robot displacement shown in figs. S4 to S6, we stimulated the robots over 10 thermal cycles, turned them around, and stimulated them for 10 additional thermal cycles.

Finite element analysis

We used FEA to investigate the crawling mechanism of the two-segment robot with a flexible linker. We applied the thermochemo-mechanical model of Chester *et al.* (*40*) to describe the coupled stress response and swelling behavior of the pNIPAM and pAAM hydrogels. The model was implemented as a user element subroutine in ABAQUS Unified FEA (*43*). A detailed description of the thermo-chemo-mechanical model and its finite element implementation can be found in the Supplementary Materials.

Briefly, we assumed in the model that the free energy density of the hydrogel can be decomposed additively into a mechanical part for the entropic behavior of the polymer network and a chemical part for the mixing of the solvent and polymer network. We used a compressible Neo-Hookean potential to describe the mechanical part and the Flory-Huggins potential to describe the chemical part (*44*). To model the LCST-driven thermal response, we assumed that the Flory-Huggins parameter increased with temperature from a low value for the swollen hydrophilic state to a high value for the deswollen hydrophobic state according to a sigmoidal function. The stress response of the gel and the chemical potential of the solvent are defined as the partial derivative of the free energy density with respect to the deformation and solvent concentration. We assumed a linear relationship between the solvent flux and the gradient of chemical potential to describe the stress-coupled solvent transport into the hydrogel. The stress response was determined from the mechanical equilibrium equation. The model was implemented into ABAQUS Unified FEA and applied to solve for the swelling and stress response of the hydrogel bilayers and robots.

The model contains 10 parameters: the shear modulus, the bulk modulus, the Flory-Huggins interaction parameters at a high and a low temperature, the LCST transition temperatures, the temperature range of the LCST transition, the swelling and deswelling diffusivities, the atomic volume of the solvent, and the reference chemical potential of the solvent. We obtained the values for the shear modulus of the hydrogels from dynamic mechanical characterizations performed in a previous study (*10*). We simulated the time-dependent swelling-induced bending of the bilayers with different thickness ratios to calibrate the Flory-Huggins interaction parameters at the low and the high temperature, the transition temperature, the temperature range of the transition, and the swelling and deswelling diffusivities (table S2) as described in the Supplementary Materials.

We used the obtained model parameters (table S4) to simulate the two-segment robot with either a flexible linker or a short stiff linker lying on a frictional rigid surface as described in the Supplementary Materials. The simulations also included the effects of gravity and buoyancy on the robot. We applied a temperature profile similar to the experiment shown in fig. S10. The simulations calculated the displacements at the center of the linker and the bilayers and the normal contact force for each segment.

Supplementary Materials

This PDF file includes:
Supplementary Text
Fig. S1 to S15
Table S1 to S4
References (*45–51*)

Other Supplementary Material for this manuscript includes the following:
Movie S1 to S6

REFERENCES AND NOTES

1. L. Ricotti, B. Trimmer, A. W. Feinberg, R. Raman, K. K. Parker, R. Bashir, M. Sitti, S. Martel, P. Dario, A. Menciassi, Biohybrid actuators for robotics: A review of devices actuated by living cells. *Sci Robot.* **2**, (2017).
2. M. Cianchetti, C. Laschi, A. Menciassi, P. Dario, Biomedical applications of soft robotics. *Nat. Rev. Mater.* **3**, 143–153 (2018).

3. O. Erol, A. Pantula, W. Liu, D. H. Gracias, Transformer hydrogels: A review. *Adv. Mater. Technol.* **4**, 1900043 (2019).
4. L. Hines, K. Petersen, G. Z. Lum, M. Sitti, Soft actuators for small-scale robotics. *Adv. Mater.* **29**, (2017).
5. M. A. C. Stuart, W. T. S. Huck, J. Genzer, M. Müller, C. Ober, M. Stamm, G. B. Sukhorukov, I. Szleifer, V. V. Tsukruk, M. Urban, F. Winnik, S. Zauscher, I. Luzinov, S. Minko, Emerging applications of stimuli-responsive polymer materials. *Nat. Mater.* **9**, 101–113 (2010).
6. X. Liu, J. Liu, S. Lin, X. Zhao, Hydrogel machines. *Mater. Today* **36**, 102–124 (2020).
7. L. Tan, A. C. Davis, D. J. Cappelleri, Smart polymers for microscale machines. *Adv. Funct. Mater.* **31**, 2007125 (2021).
8. T.-Y. Huang, H. Gu, B. J. Nelson, Increasingly intelligent micromachines. *Annu. Rev. Control Robot. Auton. Syst.* **5**, 279–310 (2022).
9. H. Yuk, S. Lin, C. Ma, M. Takaffoli, N. X. Fang, X. Zhao, Hydraulic hydrogel actuators and robots optically and sonically camouflaged in water. *Nat. Commun.* **8**, 14230 (2017).
10. J. Liu, O. Erol, A. Pantula, W. Liu, Z. Jiang, K. Kobayashi, D. Chatterjee, N. Hibino, L. H. Romer, S. H. Kang, T. D. Nguyen, D. H. Gracias, Dual-gel 4D printing of bioinspired tubes. *ACS Appl. Mater. Interfaces* **11**, 8492–8498 (2019).
11. M. Li, A. Pal, A. Aghakhani, A. Pena-Francesch, M. Sitti, Soft actuators for real-world applications. *Nat. Rev. Mater.* **7**, 235–249 (2022).
12. K. Jain, R. Vedarajan, M. Watanabe, M. Ishikiriyama, N. Matsumi, Tunable LCST behavior of poly(*N*-isopropylacrylamide/ionic liquid) copolymers. *Polym. Chem.* **6**, 6819–6825 (2015).
13. K. Kobayashi, S. H. Oh, C. Yoon, D. H. Gracias, Multitemperature responsive self-folding soft biomimetic structures. *Macromol. Rapid Commun.* **39**, (2018).
14. S. Maeda, Y. Hara, T. Sakai, R. Yoshida, S. Hashimoto, Self-walking gel. *Adv. Mater.* **19**, 3480–3484 (2007).
15. H. Arora, R. Malik, L. Yeghiazarian, C. Cohen, U. Wiesner, Earthworm inspired locomotive motion from fast swelling hybrid hydrogels. *J. Polym. Sci., Part A: Polym. Chem.* **47**, 5027–5033 (2009).
16. J. Kim, S. E. Chung, S.-E. Choi, H. Lee, J. Kim, S. Kwon, Programming magnetic anisotropy in polymeric microactuators. *Nat. Mater.* **10**, 747–752 (2011).
17. F. Vernerey, T. Shen, The mechanics of hydrogel crawlers in confined environment. *J. R. Soc. Interface* **14**, 20170242 (2017).
18. T. Shen, M. G. Font, S. Jung, M. L. Gabriel, M. P. Stoykovich, F. J. Vernerey, Remotely triggered locomotion of hydrogel mag-bots in confined spaces. *Sci. Rep.* **7**, 16178 (2017).
19. G. Gao, Z. Wang, D. Xu, L. Wang, T. Xu, H. Zhang, J. Chen, J. Fu, Snap-buckling motivated controllable jumping of thermo-responsive hydrogel bilayers. *ACS Appl. Mater. Interfaces* **10**, 41724–41731 (2018).
20. A. W. Feinberg, A. Feigel, S. S. Shevkoplyas, S. Sheehy, G. M. Whitesides, K. K. Parker, Muscular thin films for building actuators and powering devices. *Science* **317**, 1366–1370 (2007).
21. V. Chan, K. Park, M. B. Collens, H. Kong, T. A. Saif, R. Bashir, Development of miniaturized walking biological machines. *Sci. Rep.* **2**, 857 (2012).
22. A. S. Gladman, E. A. Matsumoto, R. G. Nuzzo, L. Mahadevan, J. A. Lewis, Biomimetic 4D printing. *Nat. Mater.* **15**, 413–418 (2016).
23. Y. Mao, Z. Ding, C. Yuan, S. Ai, M. Isakov, J. Wu, T. Wang, M. L. Dunn, H. J. Qi, 3D printed reversible shape changing components with stimuli responsive materials. *Sci. Rep.* **6**, 24761 (2016).
24. Q. Ge, A. H. Sakhaei, H. Lee, C. K. Dunn, N. X. Fang, M. L. Dunn, Multimaterial 4D printing with tailorable shape memory polymers. *Sci. Rep.* **6**, 31110 (2016).
25. S. E. Bakarich, R. Gorkin, S. Naficy, R. Gately, M. i. H. Panhuis, G. M. Spinks, 3D/4D printing hydrogel composites: A pathway to functional devices. *MRS Adv.* **1**, 521–526 (2016).
26. J. Guo, R. Zhang, L. Zhang, X. Cao, 4D printing of robust hydrogels consisted of agarose nanofibers and polyacrylamide. *ACS Macro Lett.* **7**, 442–446 (2018).
27. Y. Jin, Y. Shen, J. Yin, J. Qian, Y. Huang, Nanoclay-based self-supporting responsive nanocomposite hydrogels for printing applications. *ACS Appl. Mater. Interfaces* **10**, 10461–10470 (2018).
28. M. Schaffner, J. A. Faber, L. Pianegonda, P. A. Rühs, F. Coulter, A. R. Studart, 3D printing of robotic soft actuators with programmable bioinspired architectures. *Nat. Commun.* **9**, 878 (2018).
29. J. Liu, W. Liu, A. Pantula, Z. Wang, D. H. Gracias, T. D. Nguyen, Periodic buckling of soft 3D printed bioinspired tubes. *Extreme Mech. Lett.* **30**, 100514 (2019).
30. E. R. Trueman, *The Locomotion of Soft-bodied Animals* (Edward Arnold, 1975).
31. S. Hirose, H. Yamada, Snake-like robots [Tutorial]. *IEEE Robot. Autom. Mag.* **16**, 88–98 (2009).
32. R. D. Maladen, Y. Ding, C. Li, D. I. Goldman, Undulatory swimming in sand: Subsurface locomotion of the sandfish lizard. *Science* **325**, 314–318 (2009).
33. Y. Tanaka, K. Ito, T. Nakagaki, R. Kobayashi, Mechanics of peristaltic locomotion and role of anchoring. *J. R. Soc. Interface* **9**, 222–233 (2012).
34. S. Kuroda, I. Kunita, Y. Tanaka, A. Ishiguro, R. Kobayashi, T. Nakagaki, Common mechanics of mode switching in locomotion of limbless and legged animals. *J. R. Soc. Interface* **11**, 20140205 (2014).
35. J. Aguilar, T. Zhang, F. Qian, M. Kingsbury, B. McInroe, N. Mazouchova, C. Li, R. Maladen, C. Gong, M. Travers, R. L. Hatton, H. Choset, P. B. Umbanhowar, D. I. Goldman, A review on locomotion robophysics: The study of movement at the intersection of robotics, soft matter and dynamical systems. *Rep. Prog. Phys.* **79**, 110001 (2016).
36. A. J. Ijspeert, A. Crespi, D. Ryczko, J.-M. Cabelguen, From swimming to walking with a salamander robot driven by a spinal cord model. *Science* **315**, 1416–1420 (2007).
37. A. J. Easteal, W. E. Price, L. A. Woolf, Diaphragm cell for high-temperature diffusion measurements. tracer diffusion coefficients for water to 363 K. *J. Chem. Soc. Faraday Trans.* **85**, 1091–1097 (1989).
38. T. Tanaka, E. Sato, Y. Hirokawa, S. Hirotsu, J. Peetermans, Critical kinetics of volume phase transition of gels. *Phys. Rev. Lett.* **55**, 2455–2458 (1985).
39. Y. Lu, K. Zhou, Y. Ding, G. Zhang, C. Wu, Origin of hysteresis observed in association and dissociation of polymer chains in water. *Phys. Chem. Chem. Phys.* **12**, 3188–3194 (2010).
40. S. A. Chester, L. Anand, A thermo-mechanically coupled theory for fluid permeation in elastomeric materials: Application to thermally responsive gels. *J. Mech. Phys. Solids* **59**, 1978–2006 (2011).
41. R. Simič, M. Yetkin, K. Zhang, N. D. Spencer, Importance of hydration and surface structure for friction of acrylamide hydrogels. *Tribol. Lett.* **68**, 64 (2020).
42. A. P. Liu, E. A. Appel, P. D. Ashby, B. M. Baker, E. Franco, L. Gu, K. Haynes, N. S. Joshi, A. M. Kloxin, P. H. J. Kouwer, J. Mittal, L. Morsut, V. Noireaux, S. Parekh, R. Schulman, S. K. Y. Tang, M. T. Valentine, S. L. Vega, W. Weber, N. Stephanopoulos, O. Chaudhuri, The living interface between synthetic biology and biomaterial design. *Nat. Mater.* **21**, 390–397 (2022).
43. S. A. Chester, C. V. Di Leo, L. Anand, A finite element implementation of a coupled diffusion-deformation theory for elastomeric gels. *Int. J. Solids Struct.* **52**, 1–18 (2015).
44. P. J. Flory, Thermodynamics of high polymer solutions. *J. Chem. Phys.* **10**, 51–61 (1942).
45. D. Bonn, S. Tanase, B. Abou, H. Tanaka, J. Meunier, Laponite: Aging and shear rejuvenation of a colloidal glass. *Phys. Rev. Lett.* **89**, 015701 (2002).
46. Q. Wang, Y. Zhao, Y. Yang, H. Xu, X. Yang, Thermosensitive phase behavior and drug release of in situ gelable poly(*N*-isopropylacrylamide-*co*-acrylamide) microgels. *Colloid Polym. Sci.* **285**, 515–521 (2007).
47. C. Love, E. D. Rainville, *Differential and Integral Calculus* (Macmillan Company, ed. 6, 1962).
48. W. Hong, X. Zhao, J. Zhou, Z. Suo, A theory of coupled diffusion and large deformation in polymeric gels. *J. Mech. Phys. Solids* **56**, 1779–1793 (2008).
49. S. A. Chester, L. Anand, A coupled theory of fluid permeation and large deformations for elastomeric materials. *J. Mech. Phys. Solids* **58**, 1879–1906 (2010).
50. C. Yoon, R. Xiao, J. Park, J. Cha, T. D. Nguyen, D. H. Gracias, Functional stimuli responsive hydrogel devices by self-folding. *Smart Mater. Struct.* **23**, 094008 (2014).
51. J. G. Choi, H. Gwac, Y. Jang, C. Richards, H. Warren, G. Spinks, S. J. Kim, Poly(*N*-isopropylacrylamide) hydrogel for diving/surfacing device. *Micromachines* **12**, 210 (2021).

Acknowledgments

Funding: Research reported in this publication was supported by the NSF (EFMA-1830893). We thank R. Schulman for discussions. **Author contributions:** D.H.G., N.J.C., T.D.N., J.L., S.D., and A.P. conceptualized the study and robot designs. A.P. fabricated the robots, collected the data, and created the videos under the supervision of D.H.G. B.D., Y.S., and J.L. performed FEA simulations and mechanism studies under the supervision of T.D.N. M.W. designed the schematics used in the figures. A.P., B.D., S.D., N.J.C. T.D.N., and D.H.G. wrote the manuscript with input and edits from all authors. **Competing interests:** The authors declare that they have no competing interests. **Data and materials availability:** All data needed to evaluate the conclusions in the paper are present in the paper or the Supplementary Materials.

Submitted 2 June 2022
Accepted 21 November 2022
Published 14 December 2022
10.1126/scirobotics.add2903

Science Robotics

Untethered unidirectionally crawling gels driven by asymmetry in contact forces

Aishwarya Pantula, Bibekananda Datta, Yupin Shi, Margaret Wang, Jiayu Liu, Siming Deng, Noah J. Cowan, Thao D. Nguyen, and David H. Gracias

Sci. Robot., **7** (73), eadd2903.
DOI: 10.1126/scirobotics.add2903